

## Article

# Modulated Monoclinic Hydroxyapatite: The Effect of pH in the Microwave Assisted Method

Daniel Sánchez-Campos<sup>1</sup>, Maria Isabel Reyes Valderrama<sup>1</sup> , Susana López-Ortiz<sup>1</sup>, Daniela Salado-Leza<sup>2</sup> , María Eufemia Fernández-García<sup>3</sup>, Demetrio Mendoza-Anaya<sup>3,\*</sup> , Eleazar Salinas-Rodríguez<sup>1</sup>  and Ventura Rodríguez-Lugo<sup>1,\*</sup> 

<sup>1</sup> Área Académica de Ciencias de la Tierra y Materiales, Instituto de Ciencias Básicas e Ingeniería, Universidad Autónoma del Estado de Hidalgo, Carretera Pachuca-Tulancingo Km. 4.5, Pachuca 42184, Mexico; audio.daniel@hotmail.com (D.S.-C.); isareyv@hotmail.com (M.I.R.V.); multimediassusy@hotmail.com (S.L.-O.); salinasr@uaeh.edu.mx (E.S.-R.)

<sup>2</sup> Cátedras CONACYT, Facultad de Ciencias Químicas, Universidad Autónoma de San Luis Potosí, San Luis Potosí 78210, Mexico; daniela.salado@conacyt.mx

<sup>3</sup> Instituto Nacional de Investigaciones Nucleares, Carretera Mexico-Toluca S/N La Marquesa, Ocoyoacac 52750, Mexico; maria.fernandez@inin.gob.mx

\* Correspondence: demetrio.mendoza@inin.gob.mx (D.M.-A.); ventura.rl65@gmail.com (V.R.-L.)



**Citation:** Sánchez-Campos, D.; Reyes Valderrama, M.I.; López-Ortiz, S.; Salado-Leza, D.; Fernández-García, M.E.; Mendoza-Anaya, D.; Salinas-Rodríguez, E.; Rodríguez-Lugo, V. Modulated Monoclinic Hydroxyapatite: The Effect of pH in the Microwave Assisted Method. *Minerals* **2021**, *11*, 314. <https://doi.org/10.3390/min11030314>

Academic Editors: Rafael Santos and Ricardo Jeldres

Received: 4 February 2021

Accepted: 15 March 2021

Published: 17 March 2021

**Publisher's Note:** MDPI stays neutral with regard to jurisdictional claims in published maps and institutional affiliations.



**Copyright:** © 2021 by the authors. Licensee MDPI, Basel, Switzerland. This article is an open access article distributed under the terms and conditions of the Creative Commons Attribution (CC BY) license (<https://creativecommons.org/licenses/by/4.0/>).

**Abstract:** Hydroxyapatite (HAp) is a natural hard tissue constituent widely used for bone and tooth replacement engineering. In the present work, synthetic HAp was obtained from calcium nitrate tetrahydrate ( $\text{Ca}(\text{NO}_3)_2 \cdot 4\text{H}_2\text{O}$ ) and ammonium phosphate dibasic ( $(\text{NH}_4)_2\text{HPO}_4$ ) following an optimized microwave assisted hydrothermal method. The effect of pH was evaluated by the addition of ammonium hydroxide ( $\text{NH}_4\text{OH}$ ). Hence, different characterization techniques were used to determine its influence on the resulted HAp powders' size, shape, and crystallinity. By Transmission Electron Microscopy (TEM), it was observed that the reaction pH environment modifies the morphology of HAp, and a shape evolution, from sub-hedral particles at pH = 7 to rod-like nanosized HAp at pH = 10, was confirmed. Using the X-ray Diffraction (XRD) technique, the characteristic diffraction peaks of the monoclinic phase were identified. Even if the performed Rietveld analysis indicated the presence of both phases (hexagonal and monoclinic), monoclinic HAp prevails in 95% with an average crystallite size of about 23 nm. The infrared spectra (FTIR) showed absorption bands at  $3468\text{ cm}^{-1}$  and  $630\text{ cm}^{-1}$  associated with  $\text{OH}^-$  of hydroxyapatite, and bands at  $584\text{ cm}^{-1}$ ,  $960\text{ cm}^{-1}$ , and  $1090\text{ cm}^{-1}$  that correspond to the  $\text{PO}_4^{3-}$  and  $\text{CO}_3^{2-}$  characteristic groups. In summary, this work contributes to obtaining nanosized rod-like monoclinic HAp by a simple and soft method that has not been previously reported.

**Keywords:** hydroxyapatite; microwave hydrothermal synthesis; pH effect; hydroxyapatite nanorods; monoclinic phase

## 1. Introduction

In the last few decades, the development of synthetic hydroxyapatite (HAp) ( $\text{Ca}_{10}(\text{PO}_4)_6(\text{OH})_2$ ) has gained enormous scientific interest due to its unique characteristics, such as excellent biocompatibility [1], bioactivity [2], osteoconduction [3], chemical stability, and potential use as a filling material [4]. Indeed, natural HAp is considered the main mineral constituent of hard tissue, which consists of 9% water, 22% organic matter, mainly collagen, and 69% inorganic matter that actually corresponds to HAp [5].

Today, HAp may be synthesized in the laboratory. Actually, a significant number of scientific reports have demonstrated that synthetic HAp shows similar crystallographic characteristics and chemical properties to naturally occurring HAp. Therefore, synthetic HAp has been widely used in bone and tooth tissue replacement and reconstruction applications, such as implant coatings and bone substitutes, among others [6,7]. HAp

can be synthesized by different routes, (i) dry methods: solid-state synthesis [8] and mechanochemical [9]; (ii) wet methods: conventional chemical precipitation, hydrolysis, sol-gel, hydrothermal, emulsion, and sonochemistry [10]; and (iii) high temperature processes: combustion and pyrolysis [11]. However, the remaining challenge consists in establishing an adequate synthesis method that allows obtaining a product with enhanced physicochemical characteristics and properties, i.e., with an exquisite crystallite and particle size control, and structure homogeneity, avoiding by-products and the appearance of new phases [12–16]. In this perspective, microwave synthesis is an alternative technique to provide autogenous thermal energy to the reaction. It presents interesting advantages, such as time and energy saving, few by-products generation, high yields, and few steps; it also worthy of mention that it supports the development of greener strategies to produce novel materials for a wide variety of applications [17]. The success of the microwave heating lies in the inherent properties of liquids and solids to convert, in situ, the microwave energy into heat and, thus, to promote chemical reactions. This conversion depends on the polarity of solvents as microwaves interact with the dipole moment of the solvents' molecules. As results, a higher heating rate is obtained in comparison with indirect heating approaches (conduction). This high rate induces an accelerated kinetic reaction in shorter time, leading to selective crystallization, formation of novel phases, and the grown of nanostructured materials. In addition, it allows savings energy consumption. For all these reasons, at present, this technique is widely used and directly related to processes, such as: digestion, drying, calcination, decomposition, and chemical sintering, among others [18–20].

Moreover, it is well known that the bioactivity of natural and synthetic HAp strongly depends on its size and shape features. For instance, it has been observed that the biocompatibility and chemical reactivity of HAp increases by decreasing its size [21]. It is worth mentioning that almost all the crystallographic analysis referring to natural and synthetic HAp have shown, exclusively, the presence of the hexagonal crystalline phase (around 97% of the scientific works related to the synthesis and characterization of HAp) [22–24], and only a few articles have reported the probable presence of monoclinic HAp [25]. Table 1 shows the main characteristics of the hexagonal and monoclinic phase found in the literature.

**Table 1.** Comparison between hydroxyapatite (Hap) phases [25–28].

Characteristic	Hexagonal HAp	Monoclinic HAp
Chemical formula	Ca <sub>5</sub> (PO <sub>4</sub> ) <sub>3</sub> OH PDF-00-009-0432	Ca <sub>5</sub> (PO <sub>4</sub> ) <sub>3</sub> (OH) PDF-01-089-4405
Space group	P63/m	P21/b
Lattice parameters unit cell	a = b = 9.432 Å, c = 6.881 Å and γ = 120°	a = 9.421 Å, b = 2a, c = 6.881 Å and γ = 120°
OH <sup>-</sup> position	Opposite direction	Same direction

In comparison with the HAp hexagonal phase, the monoclinic is thermodynamically more stable, a very important characteristic as its field of application may be widened. Some authors have reported the synthesis of monoclinic HAp by various methods. For instance, H. Morgan et al. obtained monoclinic HAp with a hexagonal shape at 900 °C [29], and T. Ikoma et al. followed a wet methodology and heated up to 1200 °C to induce the monoclinic phase. On the other hand, L. Pastero et al. used wet synthesis and citrate as surfactant to preferentially obtain monoclinic hydroxyapatite at 135 °C [30].

Therefore, the aim of this work was to synthesize monoclinic HAp through the microwave-induced hydrothermal method at softer temperature conditions than those already reported. As mentioned before, the characteristics of the final HAp highly depend on the experimental conditions (precursors nature, reaction temperature, Ca/P ratio, pH, etc.). Here, the reaction pH was chosen as main parameters due to its important effect on the chemical reaction rate. In this regard, the pH was varied from 7 to 10 to promote the for-

mation of the monoclinic HAp phase. To corroborate the monoclinic phase, complementary XRD, TEM, and FTIR techniques were used.

## 2. Materials and Methods

### 2.1. Microwave Assisted Hydrothermal Synthesis

Figure 1 schematically shows the experimental procedure used in this work to synthesize HAp. Likewise, the HAp formation may be expressed as the following equation:

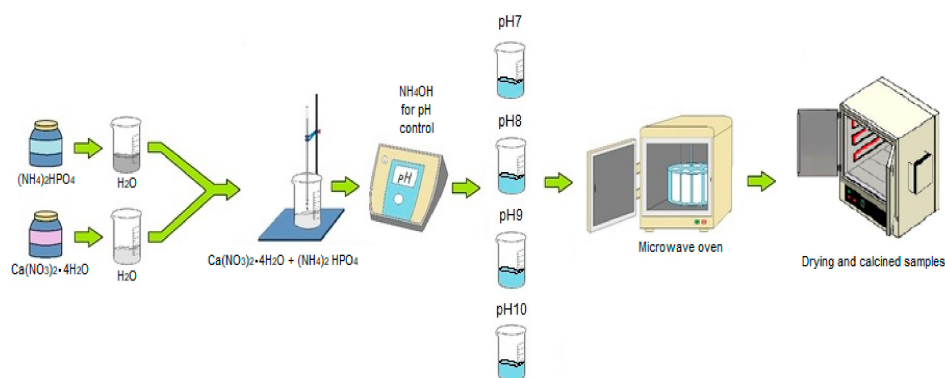
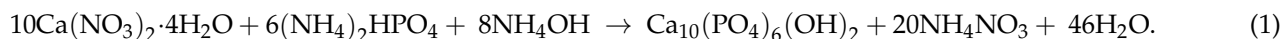


**Figure 1.** Schematic experimental protocol used to prepare synthetic HAp. The pH of the aqueous precursors' solutions was adjusted prior to performing the chemical reaction inside the microwave oven.

Briefly, stock solutions were prepared by dissolving calcium nitrate tetrahydrate ( $\text{Ca}(\text{NO}_3)_2 \cdot 4\text{H}_2\text{O}$ , 2.3662 g, Meyer analytical grade) and ammonium phosphate dibasic ( $(\text{NH}_4)_2 \cdot \text{HPO}_4$ , 0.7932 g, Meyer analytical grade) in 160.6 mL of distilled water, each. These stock solutions were then mixed dropwise and kept under stirring to produce Ca/P suspensions with stoichiometric molar ratios of 1.67. Subsequently, the solutions were brought to the desired pH (7, 8, 9, and 10) by adding ammonium hydroxide ( $\text{NH}_4\text{OH}$ , Meyer analytical grade). Finally, the suspensions at different pH were transferred to microwave-induced Teflon hydrothermal reactors (START D, Microwave Digestion System, Milestone S.R.L.) (Italian technology) keeping the temperature at 200 °C for 30 min; here, it is important to mention that the initial pH was controlled, but, once starting the chemical reaction inside the microwave oven, the pH was unchecked as the experimental procedure was performed in a closed system. At the end of the reaction, the products were washed twice with distilled water and recovered by centrifugation. Subsequently, the samples were placed in a drying oven at 80 °C for 24 h to eliminate moisture, and calcinated in a muffle at 500 °C for 4 h.

### 2.2. Physicochemical Characterization

The morphological properties were analyzed using a JEOL JEM-2010 (Japanese technology) HT Transmission Electron Microscope (TEM) with a 1.9 Å resolution. The X-ray diffraction technique (XRD) was carried out in a D8 Discover Bruker diffractometer (German technology) ( $\text{CuK}\alpha = 1.5406 \text{ \AA}$ ) operating at 40 kV and 40 mA to evaluate the HAp crystallinity. The diffractograms were obtained in a  $2\theta$  scale ranging from 10° to 70° with an incremental step size of 0.03°, and the acquisition time was set up at 2 s. The XRD patterns were refined and analyzed by the Rietveld method using the TOPAS software (Version 5, Copyright 1999-2014 Bruker AXS) [31,32] to determine the amounts (% fraction) of the different phases, as well as their effective crystallite average size. The Rietveld method allows calculating a theoretical XRD pattern, as well as matching it with the experimental diffraction pattern. The goodness of fit, between the theoretical and experimental diffractograms was determined by the weighted and expected profile ( $R_{\text{wp}}$  and  $R_{\text{exp}}$ , respectively), in which the ratio between the two (goodness of fit)  $\chi^2 = (R_{\text{wp}}/R_{\text{exp}})^2$  should approach

1. Functional groups were elucidated by Infrared spectroscopy (FTIR) using a Spectrum Gx FTIR System (Perkin Elmer) (American technology) and the attenuated total reflection technique (ATR) in a wave number range from 4000 to 400  $\text{cm}^{-1}$ .

### 3. Results

#### 3.1. The Effect of pH on the Size and Shape of HAp

The size and shape of the obtained HAp powders were evaluated by TEM. Figure 2 (left column) shows TEM micrographs where, depending on the initial reaction pH environment, different morphologies can be observed. Indeed, at pH values of 7 and 8, mainly semi-spherical (e.g., sub-hedral) particles were found, while, at the increased pH values of 9 and 10, well-defined rod-like shapes are observed.

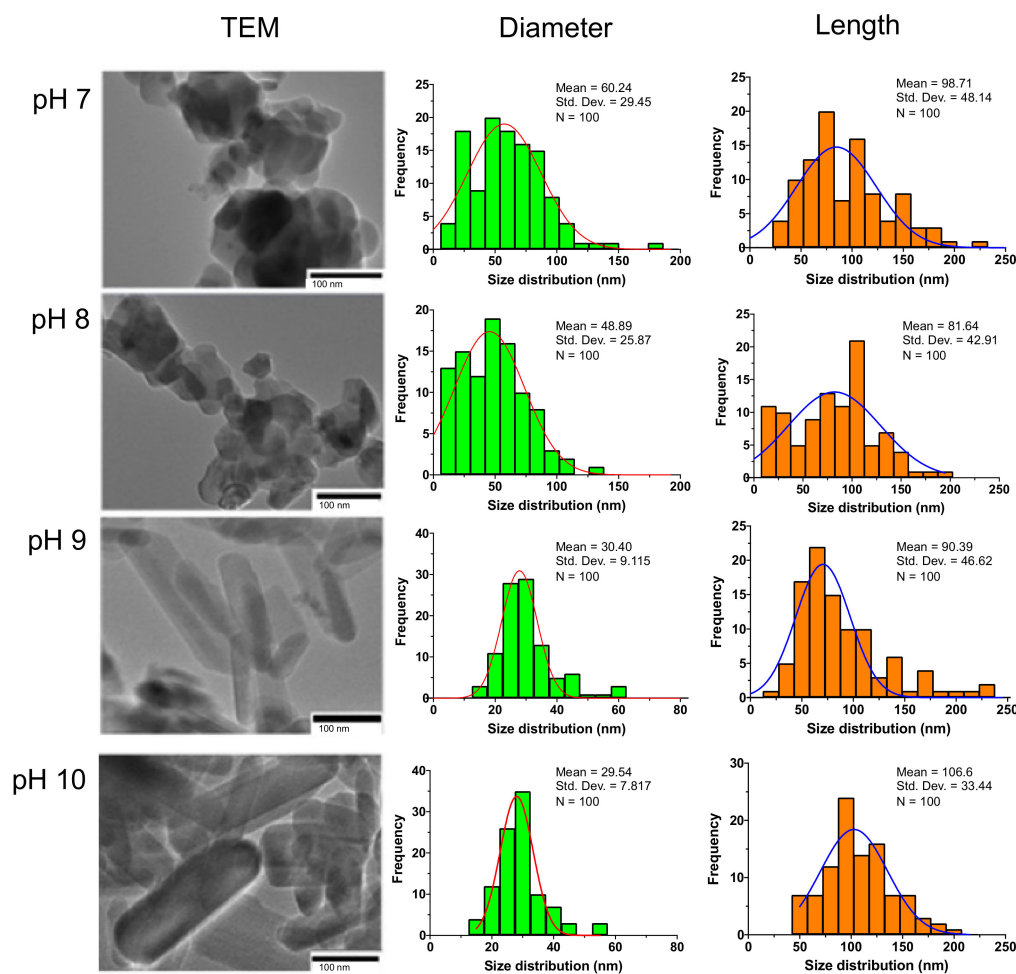


**Figure 2.** TEM micrographs of the HAp synthesized at different pH values and their corresponding diameter and length histograms (TEM scale bar: 100 nm). Depending on the initial reaction pH environment, different morphologies can be observed: standing out are the presence of semi-spherical particles for lower pH and rod-like shapes particles for higher pH.

The diameter and length size distribution histograms (middle and right columns) were built considering ca. 100 manual measurements. The average sizes (or mean)  $\pm$  standard derivations are reported in Figure 2 and summarized in Table 2. Therefore, the HAp sample prepared at initial pH = 7 contains particles with an average diameter of 60.24 nm and an average length of 98.71 nm. At this condition, the presence of sub-hedral particles was confirmed. In the sample at pH = 8, particles with an average diameter of 48.89 nm and a length of about 81.64 nm are observed. On the other hand, at pH = 9 nanorods with a length/diameter (L/D) aspect ratio close to 2.973 (higher than the circularity value of 1.0,  $L = D$ ) were formed, and it was notably observed that their radial dimension decreases by

increasing the pH. Thus, the sample obtained at a pH value of 10, shows thinner nanorods with a diameter of 29.54 nm and length of approximately 106.6 nm ( $L/D = 3.608$ ).

**Table 2.** Length/diameter (L/D) and aspect ratio of the HAp synthesized by the microwave-assisted method varying the pH.

Sample	Diameter Mean $\pm$ SD	Length Mean $\pm$ SD	Aspect Ratio L/D
pH 7	60.24 $\pm$ 29.45	98.71 $\pm$ 48.14	1.637 $\pm$ 0.001
pH 8	48.89 $\pm$ 25.87	81.64 $\pm$ 42.91	1.669 $\pm$ 0.003
pH 9	30.40 $\pm$ 9.115	90.39 $\pm$ 46.62	2.973 $\pm$ 0.494
pH 10	29.54 $\pm$ 7.817	106.6 $\pm$ 33.44	3.608 $\pm$ 0.140

The dimensional raw data were also statistically analyzed performing one-way ANOVA using a licensed Prism 8 package. The Tukey's method was applied for the multiple comparisons with a 99% confidence interval (0.01 significance). Table 3 reports the mixed-effects analysis. Briefly, we observed that the nano-objects radial dimension (diameter) significantly decrease at initial reaction pH of 9 and 10 in comparison with pH 7 and 8 ( $p$  value  $<0.0001$ ). The HAp diameter did not vary comparing pH 7–8 and pH 9–10. In contrast, non-significant difference in the axial magnitude (length) was found for most of the HAp samples. Particularly, the length significantly changed comparing pH 8 vs pH 10. In summary, the morphological characteristics of the HAp synthesized by the performed microwave assisted hydrothermal method, depend on the initial pH reaction conditions, modulating the formation of nanosized sub-hedral and rod-like HAp.

**Table 3.** Statistical analysis performed over the HAp dimensional parameters.

Test	Diameter Analysis				Adjusted $p$ Value
	Mean Difference	99.00% CI of Difference	Significant?	Summary	
pH 7 vs. pH 8	11.35	−1.869 to 24.57	No	*	0.0358
pH 7 vs. pH 9	29.84	19.99 to 39.70	Yes	****	$<0.0001$
pH 7 vs. pH 10	30.70	21.16 to 40.25	Yes	****	$<0.0001$
pH 8 vs. pH 9	18.49	9.615 to 27.37	Yes	****	$<0.0001$
pH 8 vs. pH 10	19.35	10.49 to 28.22	Yes	****	$<0.0001$
pH 9 vs. pH 10	0.8603	−3.120 to 4.840	No	ns	0.9005
Test	Length analysis				Adjusted $p$ Value
	Mean Difference	99.00% CI of Difference	Significant?	Summary	
pH 7 vs. pH 8	17.07	−1.145 to 35.29	No	*	0.0180
pH 7 vs. pH 9	8.324	−9.797 to 26.45	No	ns	0.4610
pH 7 vs. pH 10	−7.886	−26.64 to 10.87	No	ns	0.5379
pH 8 vs. pH 9	−8.751	−28.41 to 10.90	No	ns	0.4885
pH 8 vs. pH 10	−24.96	−40.98 to −8.944	Yes	****	$<0.0001$
pH 9 vs. pH 10	−16.21	−35.51 to 3.095	No	*	0.0419

CI = Confidence Intervals; \* = Identifies adjusted  $p$  values between 0.01 and 0.05; \*\*\*\* = Identifies adjusted  $p$  values  $<0.0001$ , significant difference; ns. = nonsignificant.

### 3.2. The Effect of pH on the HAp Crystallite Properties

The samples, calcinated at 500 °C, were studied by XRD to determine the effect of pH over the crystallography characteristics of hydroxyapatite. Figure 3 shows the obtained X-ray diffractograms. All the samples displayed main characteristic peaks at 25.8°, 31.7°, 32.1°, 32.9°, 34.0°, and 46.69°, which correspond, respectively, to the indexing (0 0 2), (2 1 1), (−2 2 2), (3 0 0), (2 0 2), and (2 4 2) planes of the monoclinic lattice of HAp (Powder Diffraction File-PDF No. 01-089-4405). Diffraction peaks at 22.9°, 28.13°, 28.93°, and 48.09° that correspond to the planes (1 1 1), (1 2 2), (2 1 0), and (3 2 2) were also identified and

are attributed to the planes of the hexagonal lattice of HAp (PDF card No. 00-009-0432). Specifically, for the HAp sample synthesized at pH = 7, some diffraction peaks with slightly intensities located at  $18.47^\circ$ ,  $20.16^\circ$ ,  $26.66^\circ$ ,  $27.68^\circ$ ,  $29.55^\circ$ , and  $30.10^\circ$  in 2-theta scale can be observed (black squares in Figure 3) and are associated with a calcium phosphate ( $\text{Ca}_2\text{P}_2\text{O}_7$ ) crystalline phase (PDF No. 00-33-0297), which is considered a byproduct of the chemical reaction. The insert in Figure 3 shows a magnified 2-theta scale region, between  $62.5^\circ$  and  $67.0^\circ$ , in which it is possible to appreciate the presence of both HAp crystalline phases.

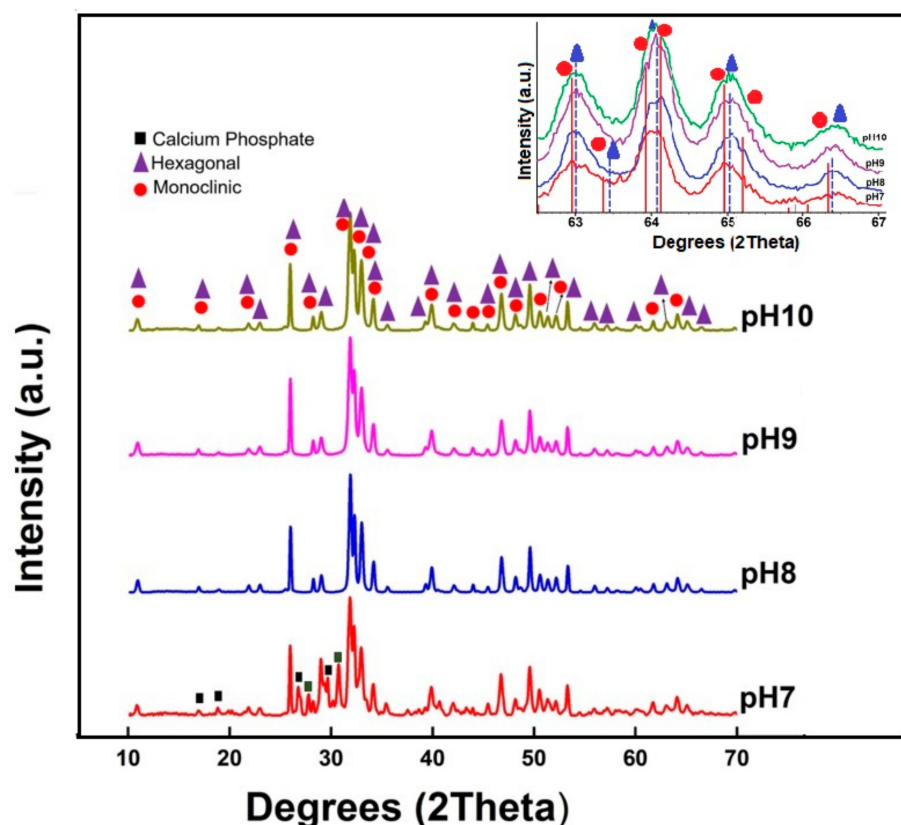


**Figure 3.** X-ray diffractograms of the HAp nanopowders synthesized at different initial pH conditions showing the presence of the calcium phosphate (■), hexagonal (▲) and monoclinic (●) HAp phases for the sample synthesized at pH = 7. Samples synthesized at pH 8, 9, and 10 showed only the presence of the monoclinic and hexagonal HAp phases. Insert: magnified region, from  $62.5^\circ$  to  $67.0^\circ$ , to appreciate the individual diffraction peaks of the monoclinic and hexagonal HAp crystalline phases.

To better elucidate the formation of monoclinic Hap, and taking into account that the XRD characteristic peaks of this phase overlap the hexagonal by geometric similarity (lattice parameters unit cell, Table 1), it was necessary to perform a Rietveld analysis to (i) identify and (ii) quantify the coexisting phases. Thus, Rietveld refinement confirms the presence of the monoclinic phase (Figure 3, orange full circles). Table 4 groups the main characteristic peaks and angles that individually identify each phase.

**Table 4.** Main planes and angles of the HAp hexagonal and monoclinic phases.

Hexagonal (PDF-00-009-0432)		Monoclinic (PDF-01-089-4405)	
Plane	Peak	Plane	Peak
(100)	10.839°	(100)	10.830°
(101)	16.846°	(101)	16.830°
(002)	25.880°	(002)	25.853°
(102)	28.131°	(102)	28.102°
(211)	31.785°	(221)	31.740°
(112)	32.201°	(222)	32.165°
(300)	32.921°	(060)	32.872°
(221)	40.463°	(023)	40.797°
(213)	49.499°	(223)	49.437°

Moreover, Table 5 summarizes the phases' contribution (%) and crystallite size (nm) obtained from the performed Rietveld analysis. The goodness of fit  $\chi^2 = (R_{wp}/R_{exp})^2$  is shown in the last column, and, for all cases, this value approaches unity, indicating that the Rietveld refinement finds a good fit. Notably, during the refinement process,  $\chi^2$  may start out large if the model is poor, and decreases as the model produces better agreement with the data [33]. Figure 4 illustrates, for the HAp sample synthesized at pH 10, its Rietveld refinement plot to support the obtained goodness of fit. In the insert, from 20° to 40° in 2-theta scale, it is possible to appreciate the individual diffraction peaks of the monoclinic HAp that, according to the Rietveld deconvolution, the peaks found at 26.431°, 27.556°, and 35.875° correspond respectively to (0 1 2), (1 1 2), and (2 7 1) hkl planes of this phase, which are forbidden for hexagonal HAp [24]. In this regard, R. Pérez-Solis et al. (2018) reported HAp with a high percentage of the monoclinic phase (80.94 wt%) obtained by means of the sol-gel method assisted by ultrasonic irradiation, and, through the use of synchrotron XRD and Rietveld refinement, they were able to quantify the presence of monoclinic and hexagonal HAp, reporting three deconvolved peaks around  $2\theta = 9.8$ ; two that corresponded to the monoclinic phase, (100) at  $2\theta = 9.873$  and (002) at  $2\theta = 9.856$ ; and another attributed to the hexagonal phase at  $2\theta = 9.785$  [34].

**Table 5.** Obtained phases and crystallite size by Rietveld analysis.

Sample	Hexagonal HAp		Monoclinic HAp		Rwp	Rexp	$\chi^2$
	Phase (%)	CrystalliteSize (nm)	Phase (%)	CrystalliteSize (nm)			
pH 7	14.96	21.3	85.04	43.80	5.81	4.68	1.54
pH 8	3.26	34.3	96.74	36.80	5.58	4.46	1.56
pH 9	3.28	38.8	96.72	26.20	5.20	4.33	1.44
pH 10	4.76	40.8	95.24	22.90	4.82	4.36	1.22

$\chi^2$ . This term is defined as a good measure of the quality of fit to a powder diffraction pattern. It is the weighted sum of the squares of the difference between the observed and calculated powder diffraction patterns [33].

In summary, in this work, we found that the monoclinic phase is the most abundant (>85%), and we observed that the crystallite's size decreases, from 43.80 nm to 22.90 nm, as the pH value increases. On the other hand, the presence of the hexagonal phase decreases, from ~15% down to ~5%, by increasing the pH. Therefore, at pH = 10, nanosized rod-like monoclinic (>95%) HAp may be successfully obtained by following this optimized soft microwave method.

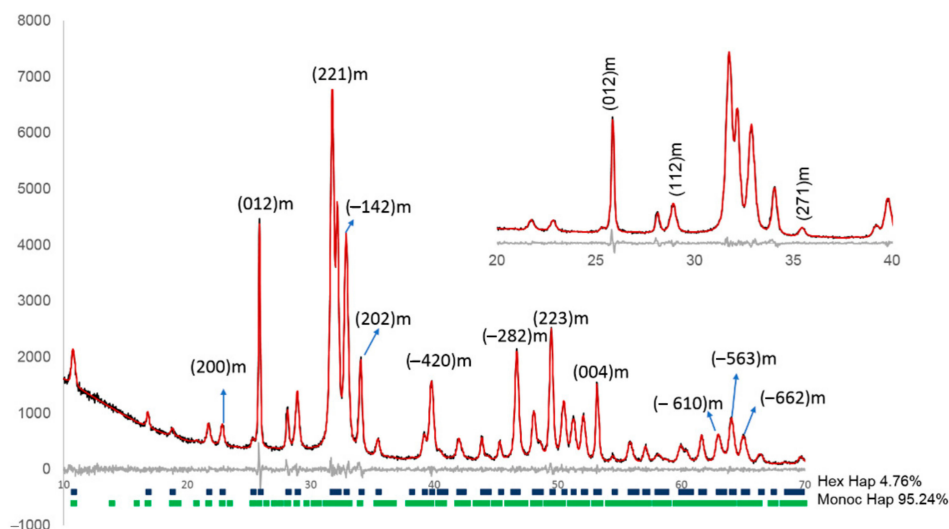


**Figure 4.** Rietveld refinement plot showing the goodness of fit obtained between the measured and calculated intensities for the HAp sample synthesized at pH 10.

### 3.3. The Effect of pH on the Presence of HAp Functional Groups

The obtained samples were complementary analyzed by FTIR. In Figure 5, the characteristic bands of HAp are observed. Firstly, the bands located at  $3570\text{ cm}^{-1}$  and  $633\text{ cm}^{-1}$  are associated with the  $\text{OH}^-$  group of hydroxyapatites. Bands at 472, 566, 603, 960, and  $1035\text{--}1092\text{ cm}^{-1}$  correspond to the  $\text{PO}_4^{3-}$  group. Likewise, it is possible to visualize bands related to the  $\text{CO}_3^{2-}$  group at 1640 and  $1950\text{ cm}^{-1}$ . The bands at lower wave numbers for the samples obtained at pH = 7 and pH = 8 are attributed to the presence of phosphate and calcium precursors that did not react during the synthesis process [35].

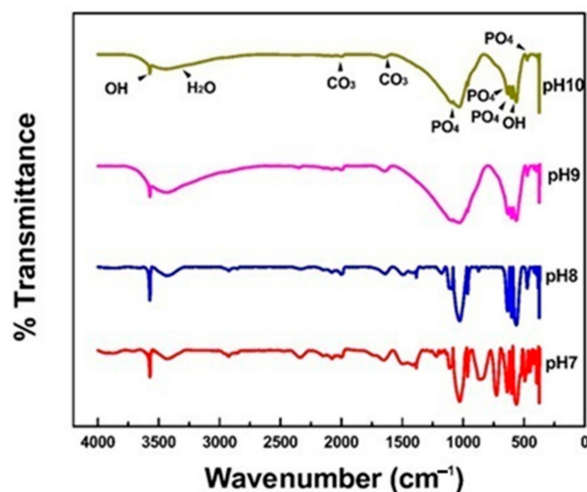


**Figure 5.** FTIR spectra of the HAp nanopowders synthesized at different initial pH values highlighting the presence of absorption bands at  $3570$  and  $633\text{ cm}^{-1}$  associated with  $\text{OH}^-$  group, and bands at 472, 566, 603, 960, and  $1035\text{--}1092\text{ cm}^{-1}$  that correspond to the  $\text{PO}_4^{3-}$  vibrational group.

According to the information in Figure 5, it is possible to visualize the main functional groups, which are summarized in Table 6, considering the region of the spectrum where they are found.

**Table 6.** Functional groups, FTIR bands, and vibrational modes identified in the HAp samples.

Functional Group	Bands	Vibrational Mode
OH <sup>-</sup>	3570 and 633 cm <sup>-1</sup>	Stretching and bending
PO <sub>4</sub> <sup>-3</sup>	472, 566, 603, 960, 1035 and 1092 cm <sup>-1</sup>	Stretching
CO <sub>3</sub> <sup>-2</sup>	1640 and 1950 cm <sup>-1</sup>	Bending

#### 4. Discussion

According to the results obtained in this work, the best condition needed to form homogeneous monoclinic hydroxyapatite nanorods, is a reaction pH of 10. To the best of the author's knowledge, here, for the first time, monoclinic HAp nanorods are obtained from such simple and soft methodology. Moreover, our experimental protocol allowed us determining the fundamental role of pH on the microstructural characteristics of HAp, contributing to better control its size, shape, and crystallographic properties.

Thus, TEM confirmed the formation of HAp nanorods with dimensions between 29 to 60 nm in diameter and 81 to 106 nm in length. Additionally, we observed that higher initial pH values induced a decrease of 50% and increase of 23%, respectively, on the average nanorod diameter and length. Indeed, the electrical balance of hydroxyapatite is affected by pH, which promotes the movement of OH<sup>-</sup> and H<sup>+</sup> ions and directly modifies the particle and crystallite structure [36]. For instance, at low pH values, agglomerates with sub-hedral particles were identified, which may be attributed to the presence of H<sup>+</sup> ions. Certainly, during the synthesis at this initial pH condition, the precursors containing solutions are unsaturated and do not promote the Ca/P nucleation to form HAp (FTIR spectrum with unreacted precursors). On the other hand, at basic pH conditions, the interaction and movement of the pending OH<sup>-</sup> groups determine the formation of any of the two HAp phases that, if they are ordered on the C-axis (determined direction), a monoclinic phase is formed [37]. Therefore, various authors have explained the role of OH<sup>-</sup> ions in determining the properties of synthetic HAp, which is mainly based on their orientation that may generate ferroelectric and electrical properties [38]. Figure 6 shows a schematic representation of the modulated growth of HAp, which varies with the increase or decrease of the pH value (increase = OH<sup>-</sup> ions; decrease = H<sup>+</sup> ions).

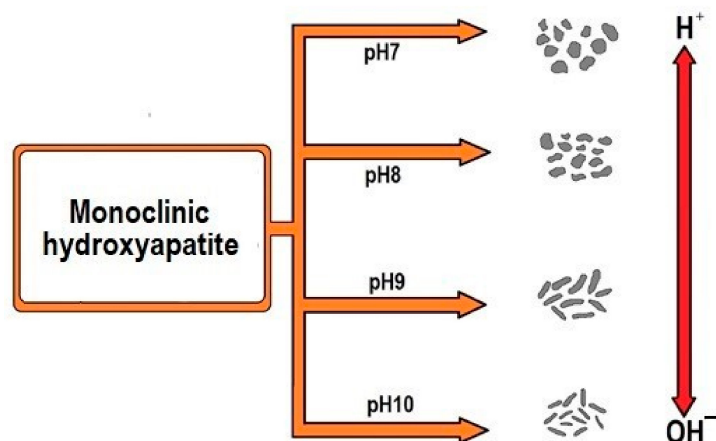


**Figure 6.** Schematic model for the H<sup>+</sup> and OH<sup>-</sup> ions effect representation on nanoparticles morphology. According to the role of OH<sup>-</sup> ions, mainly based on their orientation that may generate ferroelectric and electrical properties, this model allows showing the fundamental role of pH on the microstructural characteristics of HAp, thus contributing to better control of its size, shape and crystallographic properties.

Moreover, the crystallite size is another factor related to the presence of H<sup>+</sup> and OH<sup>-</sup> ions in solution. The Rietveld analysis confirmed a major presence of the monoclinic phase, which crystallite size decreases from about 44 to 23 nm according to the increase in OH<sup>-</sup>

ions. In the hexagonal phase, an opposite effect was observed: the crystallite size increased as the pH grew from 7 up to 11 nm. Hence, we demonstrated that, by performing a simple and soft microwave synthesis, the monoclinic phase can be obtained, thus being an important scientific contribution as the monoclinic phase is considered thermodynamically more stable than the hexagonal phase. The formation of the monoclinic phase indicates a greater order in the nucleation process, which may be translated into a better hydroxyl group internal orientation with a structural sequence of OH-OH-OH. The presence of the characteristic functional groups of pure HAp ( $\text{OH}^-$ ,  $\text{PO}_4$  and  $\text{CO}_3$ ) was confirmed by FTIR at pH = 10. Contrarily, and as mentioned before, FTIR signals attributed to unreacted HAp precursors were observed at the lower pH values of 7 and 8.

Even if other authors have reported similar HAp synthesis (Table 7), a detailed study focused on evaluating its morphology, and on identifying its crystalline phases at different pH, has been missed [39]. As shown in this work, the Rietveld refinement would be an excellent option to better elucidate the presence and contribution of each hexagonal and monoclinic HAp phases and overcome the current lack of HAp localized studies that obstructs the monoclinic phase identification [40]. Table 7 reviews the main HAp characteristics from systems obtained by similar methods. For instance, T R Amalia et al. (2020) reported the synthesis of HAp using the microwave method,  $\text{Ca}(\text{OH})_2$  and  $(\text{NH}_4)_2\text{HPO}_4$  precursors, initial pH values of 7, 9, and 11 (adjusted with HCl and NaOH), and irradiation times that varied from 15 to 25 min [41]. The authors performed an additional sintering process at 900 °C and evaluated the crystallinity, size, and morphology of the resulted HAp powders. Briefly, through the T. R. Amalia et al. (2020) methodology, round-like irregular agglomerated particles were obtained, and, contrary to our findings, an unclear shape modulation (i.e., from rounded to rod-like morphologies) was observed as a function of the pH. Particularly, they demonstrated that the additional sintering treatment increased the crystallite and particle size. Notably, at pH = 11 and prior to performing the sintering procedure, a crystallite size close to 17 nm, and an average particle size of about 63 nm, were found. After the additional treatment, they observed an important crystallite and particle size growth (~3 times). Authors reported the presence of chlorapatite at pH = 7 and 9 but did not clearly discuss either the contribution of the hexagonal or monoclinic HAp phases, assuming the presence of the conventionally reported hexagonal phase. K W Goh et al. (2020) used chicken eggshells as  $\text{CaCO}_3$  source,  $\text{H}_3\text{PO}_4$ , and  $\text{NH}_4\text{OH}$  to vary the reaction pH (8, 9, 10, 11, and 12) [42]. The microwave irradiation time was fixed to 10 min to aid the performed chemical precipitation method. At pH = 10, authors obtained needle-like shaped particles with ca. 10–15 nm in diameter and 60–80 nm in length. Authors observed that, by increasing the pH, rounded particles might be formed. Yudin et al. [43] studied the influence of the microwave treatment time (up to 30 min) and pH of the initial precursors solution over the resulting characteristics of HAp. The synthesis was performed using  $\text{Ca}(\text{NO}_3)_2$ ,  $4\text{H}_2\text{O}$ , and  $(\text{NH}_4)_2\text{HPO}_4$  at pH initial values of 8, 10, and 13 (adjusted with  $\text{NH}_4\text{OH}$ ) and 150 °C [43]. Yudin et al. [43] obtained irregular agglomerates, with a broad size distribution (0.5–25  $\mu\text{m}$ ) containing particles with sizes ranging from 17 to 46 nm. It was observed that the irradiation time induced the formation of calcium carbonate. However, authors did not specialize in identifying the hexagonal or monoclinic HAp phases, nor in the effect of pH over the crystallographic parameters. They determined that the textural properties of their agglomerates mimic the bone porosity, but the experimental procedure did not allow controlling the size and shape of the individual and aggregated HAp particles. Z-Y Cai et al. [44] reported the microwave assisted synthesis of hierarchical nanosheet-assembled HAp nanostructures (10 nm in thickness) at acidic conditions (pH = 5), rod-like HAp nanostructures (100 nm in length) at neutral (pH = 7) and alkali conditions (pH = 9), and heterogeneous structures (rods and prisms) at pH = 11 [44]. Authors used  $\text{Na}_2\text{HPO}_4 \cdot 12\text{H}_2\text{O}$ ,  $\text{Ca}(\text{CH}_3\text{COO})_2 \cdot \text{H}_2\text{O}$ , 5-fluorouracil, and HCl/NaOH to adjust the precursors pH. The reaction was carried out at 120 °C for 10 min. The HAp was identified due to its crystallographic characteristics, including tri-calcium phosphate at pH = 11. Again, even if a clear effect of the initial pH was determined and supported

by their results, no further phase's elucidation was included in the work, assuming the hexagonal phase.

**Table 7.** Results obtained with similar HAp systems from the literature.

Initial pH	Obtained Phase	Morphology	Rietveld Analysis	Reference
7, 9 and 11	Hexagonal and chlorapatite	Rounded shape	Without	[40]
8, 9, 10, 11 and 12	Hexagonal	Needle-like shape	Without	[41]
8, 10 and 13	Hexagonal and calcium carbonate	Irregular shape	Without	[42]
5, 7, 9 and 11	Hexagonal tri-calcium phosphate	Nanorods and hierarchical shape	Without	[43]

Therefore, our results and proposed methodology not only evidenced the HAp's size and shape modulation through the initial Ca/P precursors solution pH, with significant differences at pH = 10, but also include the monoclinic phase elucidation by performing the Rietveld analysis, an uncommon reported method that displays relevant information about the synthetic biomimetic nano-HAp. Finally, the stable monoclinic obtained nanostructured HAp might be used in the well-known hard tissue replacement and reconstruction applications. Other applications include drug delivery [45], cell culture, antibodies purification at large scale [46], cell activation, CO<sub>2</sub> gas sensing, catalysis, and water treatment with efficient results [47,48].

## 5. Conclusions

This work showed the effect of pH over the physicochemical main characteristics of the HAp synthesized by a microwave assisted hydrothermal method. The synthesis was performed at 200 °C, a low temperature condition that strongly differs from the conventional hydrothermal method. The obtaining of monoclinic HAp, at this low temperature and in the absence of external agents, is here reported for the first time. In brief, an increase in the monoclinic phase, from 85% to 95%, and a decrease, from 15% to 5%, in the hexagonal phase was observed according to the increase of pH. This confirmed that the monoclinic phase is a stable phase that can easily be induced by means of a simple and soft technique. The microwave assisted hydrothermal synthesis presented the following main advantages, energy saving, short processing time, high performance, economic and environmentally friendly procedure, high reproducibility, and simplicity. Finally, the synthesis pH modulated the particle and crystallite size and shape, thus being an excellent parameter to control the properties and applicability of HAp.

**Author Contributions:** Conceptualization, D.S.-C., M.I.R.V., E.S.-R. and V.R.-L.; Data curation, D.S.-C. and S.L.-O.; Formal analysis, D.S.-C., D.M.-A. and V.R.-L.; Funding acquisition, D.M.-A. and V.R.-L.; Investigation, D.S.-C., M.I.R.V., S.L.-O., D.M.-A., E.S.-R. and V.R.-L.; Methodology, D.S.-C., M.E.F.-G. and D.M.-A.; Project administration, D.M.-A. and V.R.-L.; Resources, D.M.-A. and V.R.-L.; Supervision, D.M.-A. and V.R.-L.; Validation, D.M.-A. and V.R.-L.; Visualization, D.S.-L., D.M.-A. and V.R.-L.; Writing—original draft, D.S.-C.; Writing—review & editing, D.S.-L., D.M.-A. and V.R.-L. All authors have read and agreed to the published version of the manuscript.

**Funding:** This research received no external funding.

**Data Availability Statement:** Data is contained within the article.

**Acknowledgments:** The authors are thankful to CONACYT for supporting the generation of Infrastructure through the INFR-2015-251767 project. Likewise, for the scholarships awarded belonging to the Doctorate program in Materials Sciences in the Universidad Autónoma del Estado de Hidalgo.

**Conflicts of Interest:** The authors declare no conflict of interest.

## References

1. Castaño, V.M. Controlled hydrothermal production of hydroxylapatite from marine skeletons. *Mater. Technol.* **2001**, *16*, 97–103. [CrossRef]

2. Wang, P.; Li, C.; Gong, H.; Jiang, X.; Wang, H.; Li, K. Effects of synthesis conditions on the morphology of hydroxyapatite nanoparticles produced by wet chemical process. *Powder Technol.* **2010**, *203*, 315–321. [[CrossRef](#)]
3. Rodríguez-Lugo, V.; Angeles-Chavez, C.; Mondragon, G.; Recillas-Gispert, S.; Castaño, V.M. Synthesis and structural characterization of hydroxyapatite obtained from CaO and CaHPO<sub>4</sub> by a hydrothermal method. *Mater. Res. Innov.* **2005**, *9*, 20–22. [[CrossRef](#)]
4. Rodríguez-Lugo, V.; Angeles, C.; de la Isla, A.; Castano, V.M. Effect of bio-calcium oxide on the morphology of hydroxyapatite. *Int. J. Basic Appl. Sci.* **2015**, *4*, 395. [[CrossRef](#)]
5. Zhang, X.; Vecchio, K.S. Hydrothermal synthesis of hydroxyapatite rods. *J. Cryst. Growth* **2007**, *308*, 133–140. [[CrossRef](#)]
6. Nayak, A.K. Hydroxyapatite Synthesis Methodologies: An Overview. *Int. J. ChemTech Res.* **2010**, *2*, 903–907. [[CrossRef](#)]
7. Zhang, H.; Darvell, B.W. Morphology and structural characteristics of hydroxyapatite whiskers: Effect of the initial Ca concentration, Ca/P ratio and pH. *Acta Biomater.* **2011**, *7*, 2960–2968. [[CrossRef](#)] [[PubMed](#)]
8. Chen, J.; Wen, Z.; Zhong, S.; Wang, Z.; Wu, J.; Zhang, Q. Synthesis of hydroxyapatite nanorods from abalone shells via hydrothermal solid-state conversion. *Mater. Des.* **2015**, *87*, 445–449. [[CrossRef](#)]
9. Ferro, A.C.; Guedes, M. Corrigendum to “Mechanochemical synthesis of hydroxyapatite using cuttlefish bone and chicken eggshell as calcium precursors” (*Materials Science & Engineering C* (2019) 97 (124–140), (S0928493118314589) (10.1016/j.msec.2018.11.083)). *Mater. Sci. Eng. C* **2019**, *100*, 971. [[CrossRef](#)]
10. Kim, W.; Saito, F. Sonochemical synthesis of hydroxyapatite from H<sub>3</sub>PO<sub>4</sub> solution with Ca(OH)<sub>2</sub>. *Ultrason. Sonochem.* **2001**, *8*, 85–88. [[CrossRef](#)]
11. Cho, J.S.; Lee, J.C.; Rhee, S.H. Effect of precursor concentration and spray pyrolysis temperature upon hydroxyapatite particle size and density. *J. Biomed. Mater. Res. B Appl. Biomater.* **2016**, *104*, 422–430. [[CrossRef](#)] [[PubMed](#)]
12. Elliott, J.C.; Mackie, P.E.; Young, R.A. Monoclinic hydroxyapatite. *Science* **1973**, *180*, 1055–1057. [[CrossRef](#)] [[PubMed](#)]
13. Pu’ad, N.A.S.M.; Koshy, P.; Abdullah, H.Z.; Idris, M.I.; Lee, T.C. Syntheses of hydroxyapatite from natural sources. *Heliyon* **2019**, *5*, e01588. [[CrossRef](#)]
14. Cerón, L.S.V.; Lugo, V.R.; Alatorre, J.A.A.; Fernández-García, M.E.; Reyes-Valderrama, M.I.; González-Martínez, P.; Anaya, D.M. Characterization of hap nanostructures doped with AgNp and the gamma radiation effects. *Results Phys.* **2019**, *15*, 102702. [[CrossRef](#)]
15. Szcześ, A.; Hołysz, L.; Chibowski, E. Synthesis of hydroxyapatite for biomedical applications. *Adv. Colloid Interface Sci.* **2017**, *249*, 321–330. [[CrossRef](#)] [[PubMed](#)]
16. Sadat-Shojai, M.; Khorasani, M.T.; Dinpanah-Khoshdargi, E.; Jamshidi, A. Synthesis methods for nanosized hydroxyapatite with diverse structures. *Acta Biomater.* **2013**, *9*, 7591–7621. [[CrossRef](#)] [[PubMed](#)]
17. Sánchez-Campos, D.; Mendoza-Anaya, D.; Reyes-Valderrama, M.I.; Esteban-Gómez, S.; Rodríguez-Lugo, V. Cationic surfactant at high pH in microwave HAp synthesis. *Mater. Lett.* **2020**, *265*, 3–6. [[CrossRef](#)]
18. Komarneni, S.; Katsuki, H. Nanophase materials by a novel microwave-hydrothermal process. *Pure Appl. Chem.* **2002**, *74*, 1537–1543. [[CrossRef](#)]
19. Dąbrowska, S.; Chudoba, T.; Wojnarowicz, J.; Łojkowski, W. Current trends in the development of microwave reactors for the synthesis of nanomaterials in laboratories and industries: A review. *Crystals* **2018**, *8*, 379. [[CrossRef](#)]
20. Yoshimura, M.; Byrappa, K. Hydrothermal processing of materials: Past, present and future. *J. Mater. Sci.* **2008**, *43*, 2085–2103. [[CrossRef](#)]
21. Ruys, A.J.; Wei, M.; Sorrell, C.C.; Dickson, M.R.; Brandwood, A.; Milthorpe, B.K. Sintering effects on the strength of hydroxyapatite. *Biomaterials* **1995**, *16*, 409–415. [[CrossRef](#)]
22. Hochrein, O.; Kniep, R.; Zahn, D. Atomistic simulation study of the order/disorder (monoclinic to hexagonal) phase transition of hydroxyapatite. *Chem. Mater.* **2005**, *17*, 1978–1981. [[CrossRef](#)]
23. Manalu, J.L.; Soegijono, B.; Indrani, D.J. Characterization of Hydroxyapatite Derived from Bovine Bone. *Asian J. Appl. Sci.* **2015**, *03*. ISSN:2321-0893.
24. Reyes-Gasga, J.; Martínez-Piñero, E.L.; Brès, É.F. Crystallographic structure of human tooth enamel by electron microscopy and x-ray diffraction: Hexagonal or monoclinic? *J. Microsc.* **2012**, *248*, 102–109. [[CrossRef](#)]
25. Ma, G.; Liu, X.Y. Hydroxyapatite: Hexagonal or monoclinic? *Cryst. Growth Des.* **2009**, *9*, 2991–2994. [[CrossRef](#)]
26. López-Ortiz, S.; Mendoza-Anaya, D.; Sánchez-Campos, D.; Fernández-García, M.E.; Salinas-Rodríguez, E.; Reyes-Valderrama, M.I.; Rodríguez-Lugo, V. The pH Effect on the Growth of Hexagonal and Monoclinic Hydroxyapatite Synthesized by the Hydrothermal Method. *J. Nanomater.* **2020**, *2020*. [[CrossRef](#)]
27. Sánchez-Pastenes, E.; Reyes-Gasga, J. Point and space groups for hydroxyapatite by computer simulation of CBED electron diffraction patterns. *Microsc. Microanal.* **2003**, *9*, 1314–1315. [[CrossRef](#)]
28. Leventouri, T.; Antonakos, A.; Kyriacou, A.; Venturelli, R.; Liarokapis, E.; Perdikatsis, V. Crystal Structure Studies of Human Dental Apatite as a Function of Age. *Int. J. Biomater.* **2009**, *2009*, 1–6. [[CrossRef](#)] [[PubMed](#)]
29. Morgan, H.; Wilson, R.M.; Elliott, J.C.; Dowker, S.E.P.; Anderson, P. Preparation and characterisation of monoclinic hydroxyapatite and its precipitated carbonate apatite intermediate. *Biomaterials* **2000**, *21*, 617–627. [[CrossRef](#)]
30. Pastero, L.; Bruno, M.; Aquilano, D. About the genetic mechanisms of apatites: A survey on the methodological approaches. *Minerals* **2017**, *7*, 139. [[CrossRef](#)]
31. Coelho, A.A. *TOPAS-Academic, Version 4.1*; Coelho Software: Brisbane, QLD, Australia, 2007.

32. Cullity, B.D. *Elements of X-Ray Diffraction*, 2nd ed.; Addison-Wesley Publishing Company Inc.: Quezon City, Philippines, 1978.
33. Toby, B.H. R factors in Rietveld analysis: How good is good enough? *Powder Diffr.* **2006**, *21*, 67–70. [[CrossRef](#)]
34. Pérez-Solis, R.; Gervacio-Arciniega, J.J.; Joseph, B.; Mendoza, M.E.; Moreno, A. Synthesis and characterization of a monoclinic crystalline phase of hydroxyapatite by synchrotron X-ray powder diffraction and piezoresponse force microscopy. *Crystals* **2018**, *8*, 458. [[CrossRef](#)]
35. Salma, K.; Borodajenko, N.; Plata, A.; Berzina-Cimdina, L.; Stunda, A. Fourier Transform Infrared Spectra of Technologically Modified Calcium Phosphates. *IFMBE Proc.* **2008**, *20*, 68–71. [[CrossRef](#)]
36. Ruffini, A.; Sprio, S.; Preti, L.; Tampieri, A. Synthesis of Nanostructured Hydroxyapatite via Controlled Hydrothermal Route. *Biomater. Tissue Reconstr. Regen. Ref.* **2019**, *1*, 1–22. [[CrossRef](#)]
37. Hadrich, A.; Lautié, A.; Mhiri, T. Monoclinic to hexagonal phase transition and hydroxyl motion in calcium-lead hydroxyapatites studied by Raman spectroscopy. *J. Raman Spectrosc.* **2001**, *32*, 33–40. [[CrossRef](#)]
38. Chuprunov, K.; Yudin, A.; Lysov, D.; Kolesnikov, E.; Kuznetsov, D.; Leybo, D.; Ilinykh, I.; Godymchuk, A. The pH Level Influence on Hydroxyapatite Phase Composition Synthesized with Hydrothermal Method. *IOP Conf. Ser. Mater. Sci. Eng.* **2020**, 731. [[CrossRef](#)]
39. Liu, J.; Ye, X.; Wang, H.; Zhu, M.; Wang, B.; Yan, H. The influence of pH and temperature on the morphology of hydroxyapatite synthesized by hydrothermal method. *Ceram. Int.* **2003**, *29*, 629–633. [[CrossRef](#)]
40. Amalia, T.R.; Nurlaly, S.Y.W. Synthesis of Hidroxyapatite Using Microwave Irradiation and Sintering with Variation pH and Time. *J. Phys. Conf. Ser.* **2020**, 1505. [[CrossRef](#)]
41. Goh, K.W.; Wong, Y.H.; Ramesh, S.; Chandran, H.; Krishnasamy, S.; Sidhu, A.; Teng, W.D. Effect of pH on the properties of eggshell-derived hydroxyapatite bioceramic synthesized by wet chemical method assisted by microwave irradiation. *Ceram. Int.* **2020**. [[CrossRef](#)]
42. Yudin, A.; Ilinykh, I.; Chuprunov, K.; Kolesnikov, E.; Kuznetsov, D.; Leybo, D.; Godymchuk, A. Microwave treatment and pH influence on hydroxyapatite morphology and structure. *J. Phys. Conf. Ser.* **2019**, 1145. [[CrossRef](#)]
43. Cai, Z.Y.; Peng, F.; Zi, Y.P.; Chen, F.; Qian, Q.R. Microwave-assisted hydrothermal rapid synthesis of calcium phosphates: Structural control and application in protein adsorption. *Nanomaterials* **2015**, *5*, 1284–1296. [[CrossRef](#)] [[PubMed](#)]
44. Kattimani, V.S.; Kondaka, S.; Lingamaneni, K.P. Hydroxyapatite—Past, Present, and Future in Bone Regeneration Bone Tissue Regen. *Insights* **2016**, *7*, BTRIS36138. [[CrossRef](#)]
45. Meyer, J.L.; Nancollas, G.H. The effect of pH and temperature on the crystal growth of hydroxyapatite. *Arch. Oral Biol.* **1972**, *17*, 1623–1627. [[CrossRef](#)]
46. Ortiz, S.L.; Rodríguez-Lugo, V.; Villaseñor-Cerón, L.S.; Reyes-Valderrama, M.I.; Salado-Leza, D.E.; Mendoza-Anaya, D. El Potencial de la Hidroxiapatita Dopada como Sensor Termoluminiscente de Radiación ionizante, Pádi Boletín Científico Ciencias Básicas e Ing. *Del ICBI* **2020**, *8*, 85–90. [[CrossRef](#)]
47. Rodríguez-Lugo, V.; Karthik, T.V.K.; Mendoza-Anaya, D.; Rubio-Rosas, E.; Cerón, L.S.V.; Reyes-Valderrama, M.I.; Salinas-Rodríguez, E. Wet chemical synthesis of nanocrystalline hydroxyapatite flakes: Effect of pH and sintering temperature on structural and morphological properties. *R. Soc. Open Sci.* **2018**, *5*. [[CrossRef](#)]
48. Rodríguez-Lugo, V.; Salinas-Rodríguez, E.; Vázquez, R.A.; Alemán, K.; Rivera, A.L. Hydroxyapatite synthesis from a starfish and  $\beta$ -tricalcium phosphate using a hydrothermal method. *RSC Adv.* **2017**, *7*, 7631–7639. [[CrossRef](#)]